frontiers in Materials

ORIGINAL RESEARCH
published: 17 January 2022
doi: 10.3389/fmats.2021.820671

Improving the Sodium Storage Performance of Porous Carbon Derived From Covalent Organic Frameworks Through N, S Co-Doping

Xiaochen Zhang[1], *Zijian Zhang*[1], *Xueqi Zhang*[1], *Haiquan Sun*[2], *Quan Hu*[2] *and Haibao Wang*[2]*

[1]State Grid Beijing Chaoyang Electric Power Supply Company, Beijing, China, [2]Beijing Smart-Chip Microelectronics Technology Co., Ltd., Beijing, China

Heteroatom doping, which has long been considered as one of the most efficient approaches to significantly enhance the sodium storage ability of carbonaceous anodes, has drawn increasing attention. Compared with single doping, dual doping can introduce more defects and accelerate ionic diffusion. In addition, the synergistic effect between the dual doped atoms can significantly improve the electrochemical performances. Besides, exploring novel precursors with excellent properties, which can induce porous structure and rapid pathways for electrons/ions in the resultant carbonaceous anode, is still full of challenges. Herein, nitrogen and sulfur–co-doped urchin-like porous carbon (NSC) was fabricated through a combined strategy including carbonization and subsequent sulfidation, using covalent organic frameworks (COFs) as precursors. Because of the dual doping–endowed rich defects, high electronic conductivity, and favorable capacitive behavior, the resultant NSC exhibited excellent sodium storage performances, delivering superior sodium storage capacity (483.5 mAh g^{-1} at 0.1 A g^{-1} after 100 cycles) and excellent cycling stability up to 1,000 cycles (231.6 mAh g^{-1} at 1.0 A g^{-1}). Importantly, such remarkable electrochemical performances of the resultant carbonaceous anode may shed light on the efficient conversion of COFs to functional materials.

Keywords: nitrogen, sulfur co-doping, covalent organic frameworks, carbonaceous anodes, sodium storage, high performance

OPEN ACCESS

Edited by:
Likun Pan,
East China Normal University, China

Reviewed by:
Jinliang Li,
Jinan University, China
Xiaojie Zhang,
Huaiyin Institute of Technology, China

***Correspondence:**
Haibao Wang
whb11_22@163.com

Specialty section:
This article was submitted to Energy Materials, a section of the journal Frontiers in Materials

Received: *23 November 2021*
Accepted: *06 December 2021*
Published: *17 January 2022*

Citation:
Zhang X, Zhang Z, Zhang X, Sun H, Hu Q and Wang H (2022) Improving the Sodium Storage Performance of Porous Carbon Derived From Covalent Organic Frameworks Through N, S Co-Doping. Front. Mater. 8:820671. doi: 10.3389/fmats.2021.820671

INTRODUCTION

Because of their excellent features including long life span, high energy density, and excellent stability, lithium-ion batteries (LIBs) have become the most successful commercial batteries, which have been widely applied in various portable electronics and electric vehicles. Unfortunately, the uneven distribution and limited lithium resources on Earth, combining the increasing price of raw materials, restrict its further development and application. In this context, the development of alternatives for LIBs that based on earth-abundant materials becomes urgent. Very recently, because of the natural abundance of sodium and the similar working mechanism between LIBs and sodium-ion batteries (SIBs), more and more attention has been put on the research of SIBs (Li et al., 2019a; Liu et al., 2019). Unfortunately, the sluggish reaction kinetics owing to the large Na^+ radius (1.02 Å) leads to the degradation of SIBs upon cycling (Li et al., 2018a; Li et al., 2020a; Zheng et al., 2020; Li

et al., 2022). In this context, exploring advanced electrode materials, featuring low-cost and high-performance, plays a significant role in the development of SIBs.

Compared with the extensive and in-depth studies on the cathode materials for SIBs, the research on anode materials is relatively insufficient (Xie et al., 2019; Xie et al., 2020; Fang et al., 2021). In general, alloy anodes with high theoretical specific capacities are often accompanied by the high volume change, resulting in the pulverization of active material on the electrode and further degradation on cycling (Li et al., 2021a; Li et al., 2021b). Besides, conversion anodes, mainly metal oxides/sulfides, suffer from high working voltage and poor electronic conductivity, restricting their electrochemical performances and improvement on the energy density of the full batteries (Li et al., 2018b; Li et al., 2020b; Zhang et al., 2020; Li et al., 2021c; Wan et al., 2021; Yang et al., 2021; Zhang et al., 2022a). Carbonaceous anodes with a typical insertion mechanism possess suitable working voltage, excellent interaction with the electrolyte, and high electronic conductivity, combined with structure fabrication, which renders them to be promising anodes for SIBs (Chen et al., 2019; Li et al., 2021d).

To further enhance the sodium storage performances of carbonaceous anodes, porous structure constructing and heteroatom doping represent efficient approaches to provide high transportation pathways for electrons/ions, optimize the electronic architecture, and modify the charge distribution in the carbonaceous skeleton (Li et al., 2019b). As for the morphology controlling, three-dimensional (3D) porous carbon, two-dimensional (2D) carbon sheets, one-dimensional (1D) carbon fibers, and zero-dimensional (0D) carbon have been reported to deliver efficient sodium storage (Zhang et al., 2017; Li et al., 2021a). Particularly, 3D porous carbon, endowing with large surface area, convenient transportation pathways, self-buffering volume, and high electronic conductivity, is considered as a promising anode candidate for high-performance SIBs (Zhang et al., 2017; Chen et al., 2019; Li et al., 2019c). For instance, an *in situ* template carbonization method was developed to fabricate a novel hierarchical 3D porous carbon, which shows favorable pseudocapacitive behavior as well as high sodium storage performance in both half and full cells (Wang et al., 2018a). Besides, Elizabeth et al. (2016) developed a porous carbon using prawn shells as the precursor, and the coexistence of macropores, mesopores, and micropores in the resultant carbonaceous anodes offers facile and transport channels for Na^+, leading to the excellent performance of SIBs. As shown, the typical examples clearly demonstrate the structure advantages of the 3D porous carbons for high sodium storage performances, including hierarchically porous structure, rich pores, and high ionic/electronic conductivity.

Except for the construction of 3D porous structure, heteroatom doping, which can induce abundant defects and increase electronic conductivity of the target carbonaceous anodes, is also a feasible strategy to boost the electrochemical performance of carbonaceous anodes (Li et al., 2019b; Li et al., 2019d). Nitrogen (N), possessing a similar covalent radius with carbon, has become the star doping atom due to the fact that the introduction of N into the carbonaceous skeleton can further increase the electronic conductivity, causing the bias of electron cloud from the N atoms to the carbon atoms (Li et al., 2021e). Moreover, sulfur (S) doping, which is an efficient supplement for N doping, has also shown great promise for improving the electrochemical performances of carbonaceous anodes, resulting from the abundant defects after S doping (Li et al., 2018c; Zhang et al., 2021). Li et al. (2021a) developed a self-template method and prepared the N and S–co-doped layered carbon, where the high contents of doped heteroatoms and the improved ionic/electronic conductivity result in remarkable sodium storage. The above examples typically prove the feasibility of structure control and heteroatom doping for improving the electrochemical performances of the target electrode (Li et al., 2018d; Li et al., 2018e; Li et al., 2019e; Lu et al., 2021). In this regard, smart design and rational fabrication of a 3D porous skeleton with N and S co-doping, featuring rich defects, low charge-transfer polarization, and abundant active sites, are believed to obtain carbonaceous materials with high electrochemical performances (Zhang et al., 2017; Hong et al., 2019; Wang et al., 2020; Wang et al., 2021; Zhang et al., 2022b; Zhang et al., 2022c). However, exploring novel precursors with unique properties for the construction of 3D porous skeleton and subsequent heteroatom doping is challenging.

In this work, covalent-organic framework (COF), a new type of crystalline polymers composed of nonmetal elements (H, C, N, and O) through covalent bonding, is selected as the precursor due to their adjustable pore sizes and structures (Zhang et al., 2017). Through facile carbonization and subsequent sulfidation, N and S–co-doped urchin-like porous carbon (NSC) can be obtained. The COFs-induced urchin-like morphology and porous structure and stable inner structure, combining the heteroatoms doping induced favorable ionic/electronic conductivity and rich active sites, result in expressive sodium storage performance, showing great potential for the fabrication of high-performance SIBs.

EXPERIMENTAL

Synthesis of COFs

In a typical synthesis, 1,3,5-triformylphloroglucinol (63 mg), *p*-paraphenylenediamine (48 mg), 3 M aqueous acetic acid (0.5 ml), dioxane (1.5 ml), and mesitylene (1.5 ml) were mixed, which was then added into a Pyrex tube. After sonicating for 10 min, the sealed tube containing the uniform dispersion was heated at 120°C for 3 days. After the tube cooled down to room temperature, the red product was collected through centrifugation and washing with anhydrous acetone several times. Afterward, the product was dried under vacuum overnight to receive the desired COFs.

Synthesis of NC and NSC

To synthesize the NC, the received COFs were directly carbonized at 600°C for 4 h under N_2 protection with a heating rate of 5°C min^{-1}. Generally, the carbonized step was used to stabilize the carbonaceous skeleton, facilitating the following sulfidation treatment. Typically, NC and S powder with a mass ratio of 1: 10 was mixed and then heated at 500°C, 600°C, and 700°C for 2 h

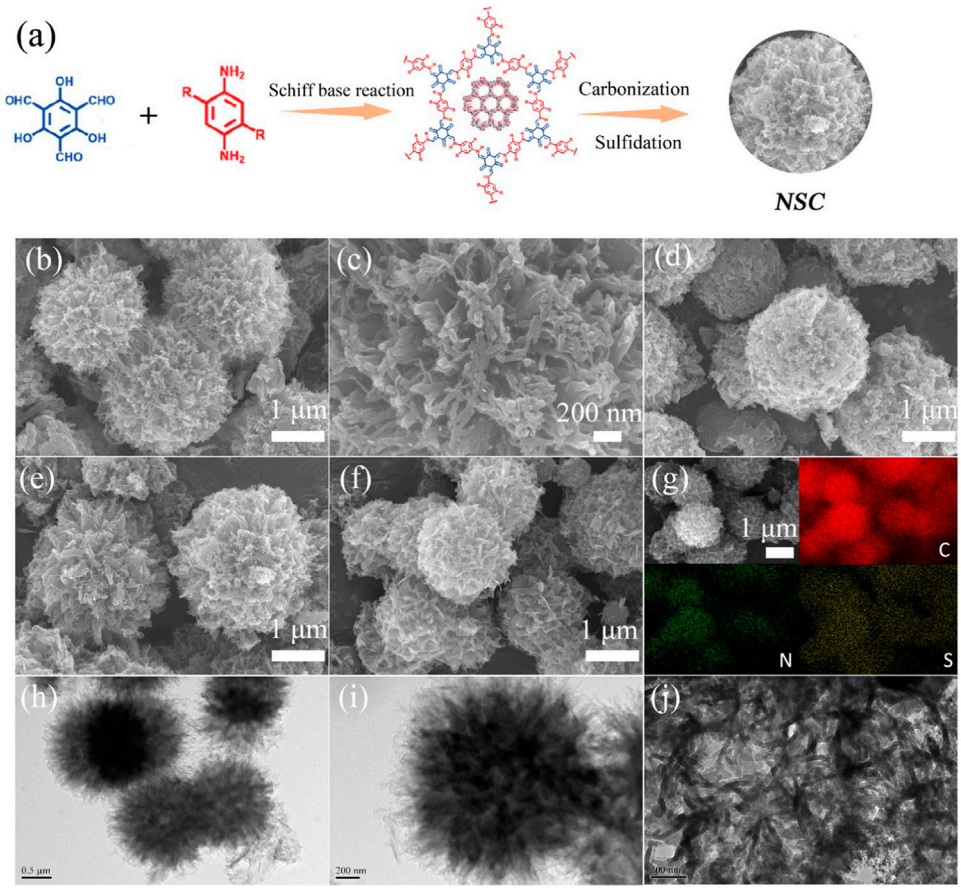

FIGURE 1 | Illustration of the conversion from as-prepared COFs to desired NSC **(A)**. FESEM images of pure COFs **(B,C)**, NSC-500 **(D)**, NSC-600 **(E),** and NSC-700 **(F)**. Elemental mapping of NSC-600 **(G)**. TEM **(H,I)** and HRTEM **(J)** images of NSC-600.

under flowing N_2 to obtain the NSC-500, NSC-600, and NSC-700, respectively.

Besides, the structure characterizations of the as-prepared samples and electrochemical methods used in this work can be found in Supporting Information (SI).

RESULTS AND DISCUSSION

As illustrated in **Figure 1A**, 1,3,5-triformylphloroglucinol and *p*-paraphenylenediamine were reacted in a Pyrex tube for 3 days at 120°C, leading to the formation of the desired COFs through Schiff-based reaction (Kandambeth et al., 2012). Besides, the further conversion from the COFs to porous carbon doped with N and S was realized through subsequent carbonization and sulfidation (Li et al., 2018c). In addition, the morphologies of the pure COFs, NSC-500, NSC-600, and NSC-700 were observed through field-emission scanning electron microscopy (FESEM, **Figures 1B–F**), from where we can detect that the morphologies of NSC-500, NSC-600, and NSC-700 maintain well compared with their precursors after the carbonization and subsequent sulfidation process. Specifically, the pure COFs possess urchin-like morphology with porous structure (**Figures 1B,C**), which is unique among COFs reported (Zhang et al., 2017; Zhang et al., 2018). As for the elemental mapping, the coexisted C, N, and S were found to be uniformly dispersed in the NSC-600, thus demonstrating the successful conversion and co-doping (**Figure 1G**) (Zhang et al., 2021; Sun et al., 2021). Further detailed observations on the structure of NSC-600 in TEM and HRTEM (**Figures 1H–J**) further confirm its urchin-like structure and homogeneous dispersion. Generally, the urchin-like sphere morphology, combined with the abundant N and S co-doping, can not only provide fast transportation pathways for the electrons/ions but also offer rich sites toward sodium storage, boosting the electrochemical performances (Augustyn et al., 2014; Dahbi et al., 2016; Wang et al., 2018b).

To detect the crystal structure of the as-prepared carbonaceous materials, X-ray diffraction (XRD) measurements were conducted (**Figure 2A**). As seen, two broad peaks corresponding to (002) and (110) planes of the graphitic frameworks can be found at around 25.0 and 43.5°, respectively (Chen et al., 2019). Besides, the (100) peak gradually increases with the increase of sulfidation temperature, meaning the increased graphitic structure in the carbonaceous skeleton (Zhang et al., 2017). Furthermore, the coexistence of disordered carbon and the graphitic domain was

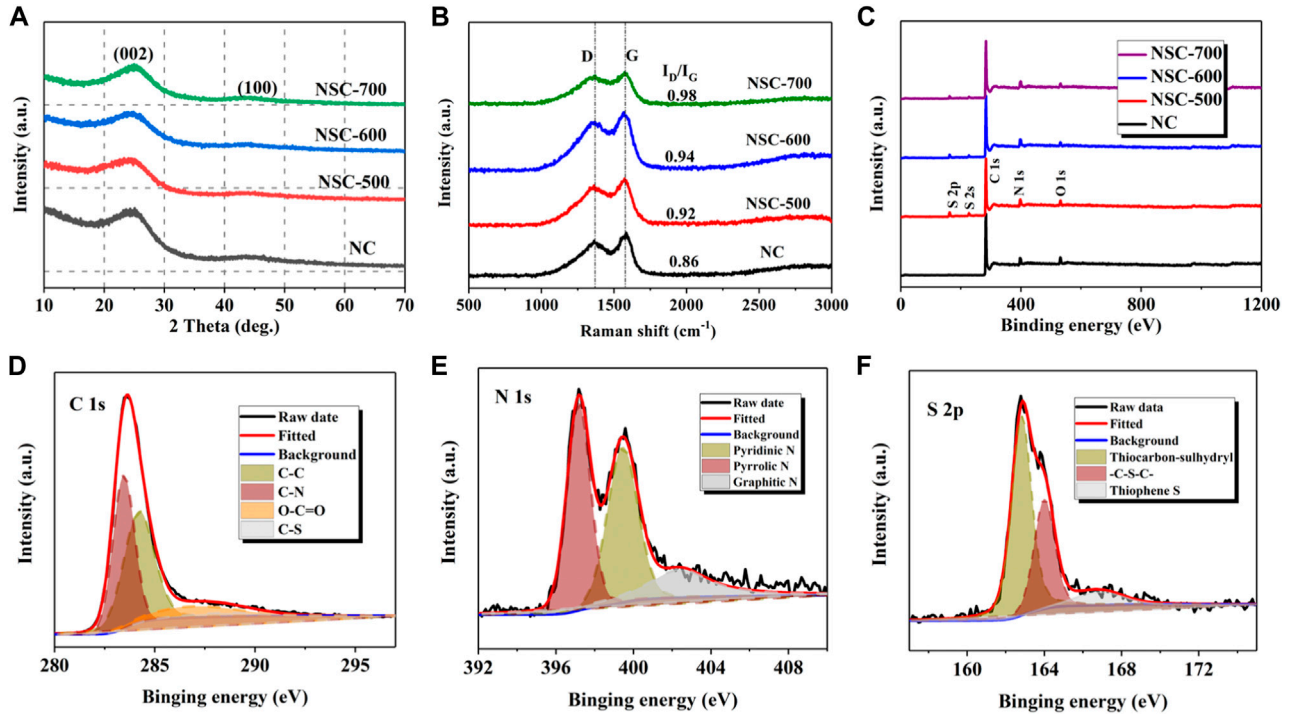

FIGURE 2 | XRD patterns **(A,B)** Raman spectra and XPS spectra **(C)** of NC, NSC-500, NSC-600, and NSC-700. High-resolution C 1s **(D)**, N 1s **(E)**, and S 2p **(F)** spectra of NSC-600.

further confirmed by the Raman spectra (**Figure 2B**), where two typical peaks ascribing to D and G bands can be clearly found at around 1,370 and 1,580 cm^{-1} (Wang et al., 2019). As known, the D band represents the characteristic feature of disordered structure in the carbonaceous skeleton, whereas the G band corresponds to the graphitic domain (Zhang et al., 2017). Moreover, the graphitization degree of the carbonaceous matrix can be estimated through the I_D/I_G value. After calculation, the I_D/I_G values for NC, NSC-500, NSC-600, and NSC-700 are 0.86, 0.92, 0.94, and 0.98, showing a slight decrease in the graphitization degree with the increasing of sulfidation temperature, which should be ascribed to the N and S co-doping–induced abundant defects in the carbonaceous skeleton (Li et al., 2019c; Wang et al., 2018a). In addition, the surface chemical components of fabricated samples were further observed through X-ray photoelectron spectroscopy (XPS). Generally, signals from C 1s, N 1s, and S 2p can be clearly observed for all the three NSC samples, whereas only C 1s and N 1s were presented for NC (**Figure 2C**). Besides, the bonding states of the C, O, and S of NSC-600 were further revealed through their high-resolution spectra (**Figures 2D–F**). **Figure 2D** illustrates the C 1s spectra of NSC-600 and the detected four peaks, with binding energies at 283.4, 284.3, 286.2, and 286.6 eV, should be assigned to the C-N, C-S, and O-C=O, respectively (Li et al., 2021a). **Figure 2E** illustrates the N 1s spectra of NSC-600, where graphitic N, pyridinic N, and pyrrolic N, respectively, are found at around 402.5, 399.5, and 397.2 eV, revealing the N atoms still remained in the carbonaceous matrix after carbonization and sulfidation (Li et al., 2019b). As for the S 2p spectrum (**Figure 2F**), three peaks at around 162.7, 164.0, and 166.9 eV correspond to thiocarbonyl-sulfhydryl, -C-S-C-, and thiophenes, respectively, demonstrating the S doping (Li et al., 2021a). For comparison, the high-resolution elemental spectra of NSC-500 and NSC-700 are shown in **Supplementary Figure S1** (SI), which displays similar deconvolved features with those of NSC-600, resulting from their analogous composition and structure.

The sodium storage ability of fabricated carbonaceous anodes was compared through various electrochemical tests, including galvanostatic discharging/charging, electrochemical impedance spectroscopy (EIS), and cyclic voltammetry (CV). First, the initial three curves of the NSC-600 electrode at the scan rate of 0.2 mV s^{-1} from 0.005 to 3.0 V are depicted in **Figure 3A**. The irreversible cathodic peak at around 0.88 V presented in the first cathodic scan, which is disappeared in the subsequent scans, should be ascribed to the decomposition of electrolyte to passivate the surface as well as the generation of solid electrolyte interface (SEI) (Eshetu et al., 2019; Cheng et al., 2021; Fan et al., 2021). In addition, another broad cathodic peak in the low voltage from 0.71 V to 0.005 V should be ascribed to the intercalation of Na^+ into the carbonaceous skeleton (Kumar et al., 2016). In the following anodic scans, only one anodic peak can be found, ascribing to the deintercalation of Na^+ (Zhang et al., 2018). After the first scan, only one pair of cathodic/anodic peaks at low voltage can be detected, manifesting reversible sodium storage, and the well-maintained CV shape reveals its good reversibility (Li and Zhang, 2018; Li et al., 2019f). Accordingly,

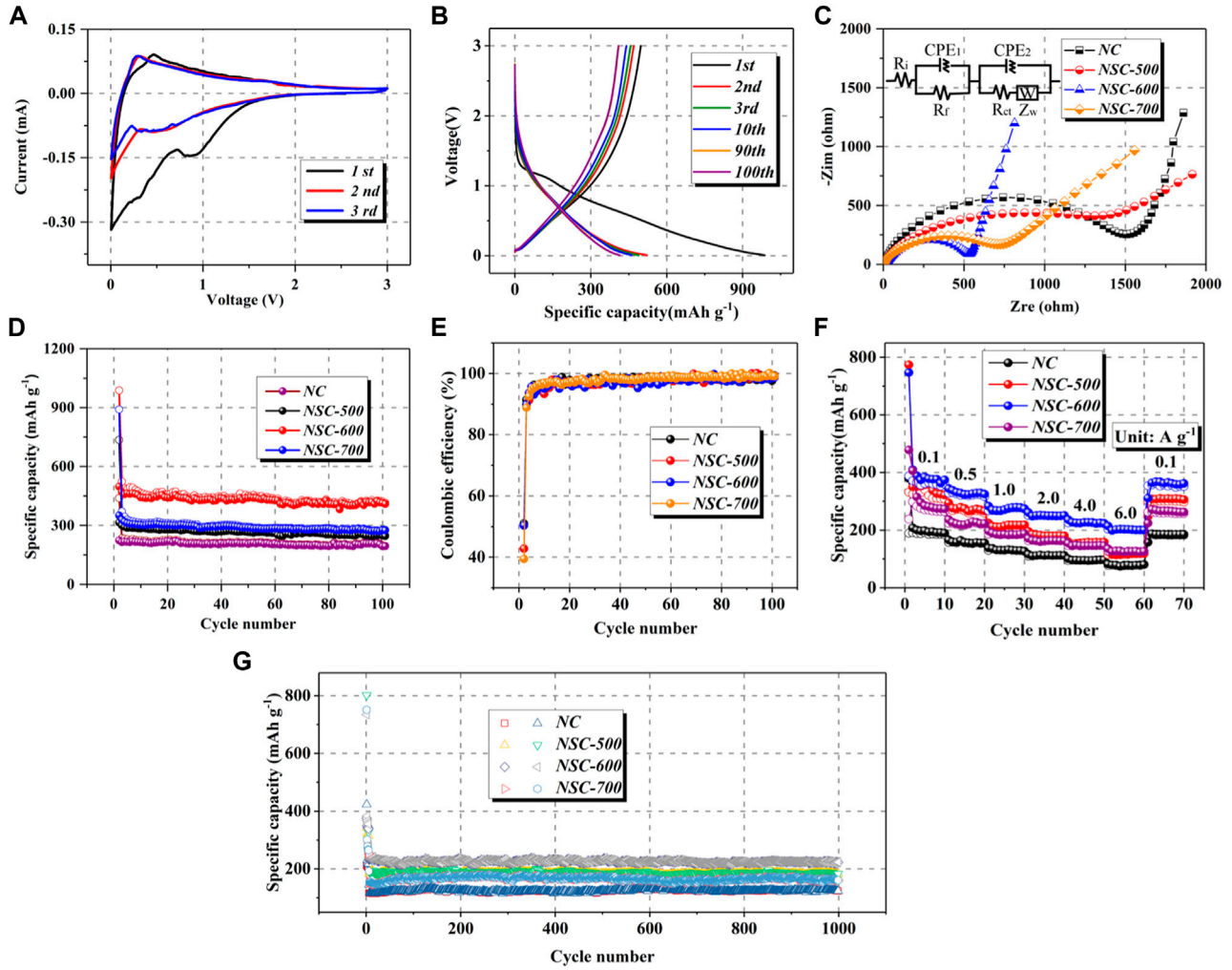

FIGURE 3 | (A) CV curves at 0.2 mV s^{-1} and **(B)** discharge/charge profiles of different cycles at 0.1 A g^{-1} for NSC-600 electrode. Electrochemical impedance spectra after five cycles **(C)**, cycling performances [0.1 A g^{-1}, **(D)**], Coulombic efficiencies **(E)**, rate performance **(F)**, and long-term cycling performance [1.0 A g^{-1}, **(G)**] of NC, NSC-500, NSC-600, and NSC-700.

the discharge/charge profiles of NSC-600 shown in **Figure 3B** further confirm its excellent electrochemical reversibility from the almost overlapped profiles. Notably, the difference on discharge profiles between the first cycle and subsequent cycles can be ascribed to the formation of SEI film due to electrolyte decomposition, structure variations and activation of electrode materials. Particularly, the first discharge/charge reversible capacities for the NSC-600 electrode are 987.5 and 497.4 mAh g^{-1}, thus acquiring an initial Coulombic efficiency of 50.4%. In general, the decomposition of electrolyte with the generation of SEI, the trapped Na^+ in electrode, and its large surface area induced some irreversible reactions contributes to the low Coulombic efficiencies (Li et al., 2020a; Zou et al., 2020). Comparatively, **Supplementary Figures S2–S4** (SI) shows the discharge/charge profiles of NC, NSC-500, and NSC-700 at 0.1 A g^{-1}, and the corresponding Coulombic efficiencies are calculated to be 51.0%, 42.8%, and 39.4% for NC, NSC-500, and NSC-700, respectively.

To detect the kinetics difference of the four samples, EIS measurements on the cycled cells were carried out, and **Figure 3C** displays the corresponding Nyquist plots. Generally, the resistance of SEI film can be detected from the small semicircle in the high-frequency region, the charge transfer resistance (R_{ct}) is related to the large semicircle in the medium-frequency region, and the ionic diffusion in the bulk electrode can be estimated from the straight line in the low-frequency region (Augustyn et al., 2014; Li et al., 2019b). Interestingly, the R_{ct} values dramatically decrease after the S doping, meaning the increased charge transfer in the NSC. Specifically, the R_{ct} values are 1,216, 536, and 756 Ω for NSC-500, NSC-600, and NSC-700, respectively. The variations on the R_{ct} values should be ascribed to their different doping contents of N and S, which have been illustrated in **Supplementary Table S1** (SI). Particularly, the N and S contents in NSC-500 are 15.68 and 10.24 at%, respectively. After increasing the sulfidation temperature to 600°C, the contents of N and S increase to 17.85 and 12.90 at%. Further

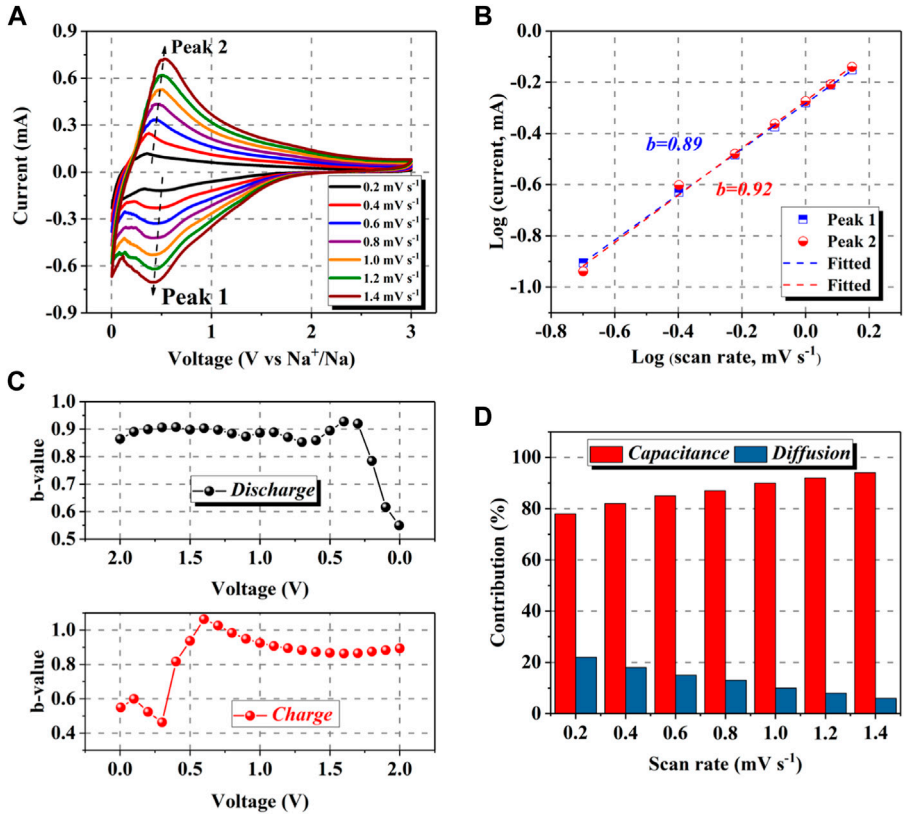

FIGURE 4 | CV curves **(A)** of NSC-600 electrode at the scan rate of 0.2–1.4 mV s^{-1}. The plots of Log(*i*) versus Log(*v*) to obtain the b values of the marked peaks in the CV curves **(B)**. The variations of b values upon discharging and charging **(C)**. Contributions at various scan rates from capacitance and diffusion **(D)**.

increasing the sulfidation temperature to 700°C results in the decrease of doping contents of N and S to 7.86 and 11.92 at%, respectively. In this context, the rich defects and decreased energy barrier for the charge transfer resulted from the high heteroatom doping contents in the carbonaceous skeleton leading to the low R_{ct} (Li et al., 2021e; Sun et al., 2021).

Comparison of the sodium storage ability among NC, NSC-500, NSC-600, and NSC-700 at 0.1 A g^{-1} is shown in **Figure 3D**. Specifically, the NSC-600 delivers the highest reversible capacity after 100 cycles (414.4 mAh g^{-1}), along with excellent cycling stability. The other three samples also demonstrate stable cycling, but the specific capacities are low, with reversible capacities of 194.5, 245.7, and 277.1 mAh g^{-1} after 100 cycles, respectively, for NC, NSC-500, and NSC-700. Besides, the high electrochemical reversibility of the electrodes was also manifested through their Coulombic efficiencies (**Figure 3E**). **Figure 3F** displays the rate capabilities of the as-prepared four samples, and the NSC-600 shows superior rate capability than the other three samples, delivering reversible capacities of 381.6, 323.9, 273.7, 250.6, 225.6, and 204.4 mAh g^{-1} at 0.1, 0.5, 1.0, 2.0, 4.0, and 6.0 A g^{-1}, respectively. Furthermore, a reversible capacity of 381.7 mAh g^{-1} can still be received after the current density returns to 0.1 A g^{-1}, showing remarkable rate capability. Moreover, further increasing the current density to 1.0 A g^{-1}, the cycling of NSC-600 electrode can still be maintained well, displaying a reversible capacity of 223.4 mAh g^{-1} after 1,000 cycles, which is the highest among the three NSC samples (182.9 mAh g^{-1} for NSC-500 and 161.2 mAh g^{-1} for NSC-700) (**Figure 3G**). The corresponding discharge/charge profiles of NSC-500, NSC-600, and NSC-700 are shown in **Supplementary Figure S5** (SI), and all the profiles show typical features of carbonaceous anodes. As shown above, the NSC exhibits superior sodium storage performance, including superior cycling stability, high specific capacity, and good rate capability. Theoretically, the urchin-like porous structure and high N, S doping contribute to the optimization of electronic/ionic conductivity, resulting in the improvement of sodium storage performance (Zhang et al., 2018; Hong et al., 2019).

To explore the dynamics mechanism upon redox reactions and the origin of the improvement on the sodium storage activity of NSC-600, CV measurements at various scan rates (0.2–1.4 mV s^{-1}) were performed to detect the charge storage kinetics (**Figure 4A**). From the CV curves obtained at various scan rates, the cathodic peak slightly shifts to the low voltage and the anodic peak shifts to the high voltage, indicating a weak polarization of electrode (Augustyn et al., 2014). According to the following equations, the charge storage in the electrode dominated by capacitance or diffusion can be determined (Li et al., 2021e).

$$i = av^b \quad (1)$$

$$\log(i) = b\log(v) + \log(a) \quad (2)$$

where i and v represent the response current and scan rate, respectively (Li et al., 2018c; Li et al., 2017). Particularly, the value of b is the typical index for the electrode kinetics upon discharging/charging (Li et al., 2021b; Li et al., 2018b). The value of b approaching 0.5 demonstrates a diffusion-dominated process, whereas the value of 1.0 manifests the redox process is controlled by capacitive behavior (Li et al., 2021a). Through plotting log(i) versus log(v) and further fitting, the b values are 0.89 and 0.92 (**Figure 4B**) for the cathodic and anodic peak marked in the CV curves, showing its favorable capacitive feature upon sodium storage, which results from its structure advantages including urchin-like morphology, porous structure, rich defects, and high doping contents (Li et al., 2021e). Further observation on the variations of b values upon discharging and charging is illustrated in **Figure 4C**. For both the discharging and charging, the variations of b demonstrate that the electrochemical process near the cathodic/anodic peak areas is dominated by capacitance, and the charge storage in areas away from the cathodic/anodic peak is controlled by capacitance (Li et al., 2021f). It is easy to understand that the variations of b values at different voltage range result from their different sodium storage mechanisms as the intercalation of Na^+ in the low voltages is promoted by diffusion, and capacitive controlled adsorption of Na^+ happens in high voltages (Li et al., 2021a; Li et al., 2021f). In addition, the charge storage contributions can be further separated into diffusion and capacitive parts through the following equations.

$$i_v = k_1 v + k_2 v^{1/2} \quad (3)$$

$$\frac{i(v)}{v^{1/2}} = k_1 v^{1/2} + k_2 \quad (4)$$

where $k_2 v^{1/2}$ and $k_1 v$ correspond to the diffusion and capacitive contributions for the charge storage, respectively (Li et al., 2021d). After detailed fitting and calculation, the contributions from capacitance and diffusion for the NSC-600 electrode are 78.1%, 81.9%, 84.9%, 87.1%, 89.8%, 91.6%, and 93.7%, respectively, at scan rates of 0.2, 0.4, 0.6, 0.8, 1.0, 1.2, and 1.4 mV s^{-1} (**Figure 4D**), manifesting favorable capacitive dominated electrochemical process, which contributes to its stable sodium storage performance (Augustyn et al., 2014).

CONCLUSION

In summary, carbonaceous skeleton co-doped with N and S was synthesized through a simple combined strategy of carbonization and subsequent sulfidation, employing novel COFs as precursors. The unique urchin-like morphology and porous structure induced efficient interaction between electrolyte and electrode; the heteroatom doping–endowed rich defects and improved electronic/ionic conductivity result in excellent sodium storage performance of the designed carbonaceous skeleton, with high reversible capacity (483.5 mAh g^{-1} at 0.1 A g^{-1} up to 100 cycles) and excellent rate capability (231.6 mAh g^{-1} at 1.0 A g^{-1} up to 1,000 cycles). This work manifests the feasibility of structure controlling and heteroatom doping to enhance the sodium storage ability of carbonaceous anodes, which shed light on the conversion of COFs to various functional materials for efficient energy storage and conversion.

DATA AVAILABILITY STATEMENT

The original contributions presented in the study are included in the article/**Supplementary Material**, further inquiries can be directed to the corresponding author.

AUTHOR CONTRIBUTIONS

XiZ: Conceptualization, Methodology, Writing original draft. ZZ: Methodology, Data curation, Investigation. XuZ: Data curation. HS: Visualization, Investigation. QH: Formal analysis. HW: Supervision, Writing–review and editing.

SUPPLEMENTARY MATERIAL

The Supplementary Material for this article can be found online at: https://www.frontiersin.org/articles/10.3389/fmats.2021.820671/full#supplementary-material

REFERENCES

Augustyn, V., Simon, P., and Dunn, B. (2014). Pseudocapacitive Oxide Materials for High-Rate Electrochemical Energy Storage. *Energy Environ. Sci.* 7 (5), 1597–1614. doi:10.1039/c3ee44164d

Chen, J., Yang, B., Hou, H., Li, H., Liu, L., Zhang, L., et al. (2019). Disordered, Large Interlayer Spacing, and Oxygen-Rich Carbon Nanosheets for Potassium Ion Hybrid Capacitor. *Adv. Energ. Mater.* 9 (19), 1803094. doi:10.1002/aenm.201970069

Cheng, D., Zhou, X., Hu, H., Li, Z., Chen, J., Miao, L., et al. (2021). Electrochemical Storage Mechanism of Sodium in Carbon Materials: A Study from Soft Carbon to Hard Carbon. *Carbon* 182, 758–769. doi:10.1016/j.carbon.2021.06.066

Dahbi, M., Yabuuchi, N., Fukunishi, M., Kubota, K., Chihara, K., Tokiwa, K., et al. (2016). Black Phosphorus as a High-Capacity, High-Capability Negative Electrode for Sodium-Ion Batteries: Investigation of the Electrode/Electrolyte Interface. *Chem. Mater.* 28 (6), 1625–1635. doi:10.1021/acs.chemmater.5b03524

Elizabeth, I., Singh, B. P., Trikha, S., and Gopukumar, S. (2016). Bio-derived Hierarchically Macro-Meso-Micro Porous Carbon Anode for Lithium/sodium Ion Batteries. *J. Power Sourc.* 329, 412–421. doi:10.1016/j.jpowsour.2016.08.106

Eshetu, G. G., Diemant, T., Hekmatfar, M., Grugeon, S., Behm, R. J., Laruelle, S., et al. (2019). Impact of the Electrolyte Salt Anion on the Solid Electrolyte Interphase Formation in Sodium Ion Batteries. *Nano Energy* 55, 327–340. doi:10.1016/j.nanoen.2018.10.040

Fan, X., Wang, Z., Cai, T., Yang, Y., Wu, H., Cao, S., et al. (2021). An Integrated Highly Stable Anode Enabled by Carbon Nanotube-Reinforced All-Carbon Binder for Enhanced Performance in Lithium-Ion Battery. *Carbon* 182, 749–757. doi:10.1016/j.carbon.2021.06.065

Fang, Z., Yin, Y., Qiu, X., Zhu, L., Dong, X., Wang, Y., et al. (2021). Prussian Blue Cathode with Intercalation Pseudocapacitive Behavior for Low-Temperature Batteries. *Adv. Energ. Sustain Res.* 7, 2100105. doi:10.1002/aesr.202100105

Hong, Y., Mao, W., Hu, Q., Chang, S., Li, D., Zhang, J., et al. (2019). Nitrogen-doped Carbon Coated SnO2 Nanoparticles Embedded in a Hierarchical Porous Carbon Framework for High-Performance Lithium-Ion Battery Anodes. *J. Power Sourc.* 428, 44–52. doi:10.1016/j.jpowsour.2019.04.093

Kandambeth, S., Mallick, A., Lukose, B., Mane, M. V., Heine, T., and Banerjee, R. (2012). Construction of Crystalline 2D Covalent Organic Frameworks with Remarkable Chemical (Acid/base) Stability via a Combined Reversible and Irreversible Route. *J. Am. Chem. Soc.* 134 (48), 19524–19527. doi:10.1021/ja308278w

Kumar, H., Detsi, E., Abraham, D. P., and Shenoy, V. B. (2016). Fundamental Mechanisms of Solvent Decomposition Involved in Solid-Electrolyte Interphase Formation in Sodium Ion Batteries. *Chem. Mater.* 28 (24), 8930–8941. doi:10.1021/acs.chemmater.6b03403

Li, J., Ding, Z., Li, J., Wang, C., Pan, L., and Wang, G. (2021). Synergistic Coupling of NiS1.03 Nanoparticle with S-Doped Reduced Graphene Oxide for Enhanced Lithium and Sodium Storage. *Chem. Eng. J.* 407, 127199. doi:10.1016/j.cej.2020.127199

Li, J., Ding, Z., Pan, L., Li, J., Wang, C., and Wang, G. (2021). Facile Self-Templating Synthesis of Layered Carbon with N, S Dual Doping for Highly Efficient Sodium Storage. *Carbon* 173, 31–40. doi:10.1016/j.carbon.2020.10.092

Li, J., Gao, W., Huang, L., Jiang, Y., Chang, X., Sun, S., et al. (2022). *In Situ* formation of Few-Layered MoS2@N-Doped Carbon Network as High Performance Anode Materials for Sodium-Ion Batteries. *Appl. Surf. Sci.* 571, 151307. doi:10.1016/j.apsusc.2021.151307

Li, J., Han, L., Li, Y., Li, J., Zhu, G., Zhang, X., et al. (2020). MXene-Decorated SnS2/Sn3S4 Hybrid as Anode Material for High-Rate Lithium-Ion Batteries. *Chem. Eng. J.* 380, 122590. doi:10.1016/j.cej.2019.122590

Li, J., Han, L., Zhang, X., Sun, H., Liu, X., Lu, T., et al. (2021). Multi-role TiO2 Layer Coated Carbon@few-Layered MoS2 Nanotubes for Durable Lithium Storage. *Chem. Eng. J.* 406, 126873. doi:10.1016/j.cej.2020.126873

Li, J., Han, L., Zhang, X., Zhu, G., Chen, T., Lu, T., et al. (2019). Sb2O5/Co-containing Carbon Polyhedra as Anode Material for High-Performance Lithium-Ion Batteries. *Chem. Eng. J.* 370, 800–809. doi:10.1016/j.cej.2019.03.244

Li, J., Li, J., Chen, T., Lu, T., Mai, W., and Pan, L. (2019). Metal Chelate Induced *In Situ* Wrapping of Ni3S2 Nanoparticles into N, S-Codoped Carbon Networks for Highly Efficient Sodium Storage. *Inorg. Chem. Front.* 6 (3), 694–704. doi:10.1039/c8qi01326h

Li, J., Li, J., Ding, Z., Zhang, X., Li, Y., Lu, T., et al. (2019). In-situ Encapsulation of Ni3S2 Nanoparticles into N-Doped Interconnected Carbon Networks for Efficient Lithium Storage. *Chem. Eng. J.* 378, 122108. doi:10.1016/j.cej.2019.122108

Li, J., Qin, W., Xie, J., Lin, R., Wang, Z., Pan, L., et al. (2018). Rational Design of MoS2-Reduced Graphene Oxide Sponges as Free-Standing Anodes for Sodium-Ion Batteries. *Chem. Eng. J.* 332, 260–266. doi:10.1016/j.cej.2017.09.088

Li, J., Tang, S., Li, Z., Wang, C., Li, J., Li, X., et al. (2021). Crosslinking Nanoarchitectonics of Nitrogen-doped Carbon/MoS 2 Nanosheets/Ti 3 C 2 T X MXene Hybrids for Highly Reversible Sodium Storage. *ChemSusChem* 14, 5293–5303. doi:10.1002/cssc.202101902

Li, J., Tang, S., Li, Z., Wang, C., and Pan, L. (2021). Boosting the Lithium Storage Performance by Synergistically Coupling Ultrafine Heazlewoodite Nanoparticle with N, S Co-doped Carbon. *J. Colloid Interf. Sci.* 604, 368–377. doi:10.1016/j.jcis.2021.07.031

Li, J., Yan, D., Hou, S., Li, Y., Lu, T., Yao, Y., et al. (2018). Improved Sodium-Ion Storage Performance of Ti3C2TxMXenes by Sulfur Doping. *J. Mater. Chem. A.* 6 (3), 1234–1243. doi:10.1039/c7ta08261d

Li, J., Yan, D., Hou, S., Lu, T., Yao, Y., Chua, D. H. C., et al. (2018). Metal-organic Frameworks Derived Yolk-Shell ZnO/NiO Microspheres as High-Performance Anode Materials for Lithium-Ion Batteries. *Chem. Eng. J.* 335, 579–589. doi:10.1016/j.cej.2017.10.183

Li, J., Yan, D., Hou, S., Lu, T., Yao, Y., and Pan, L. (2018). Metal-organic Frameworks Converted Flower-like Hybrid with Co3O4 Nanoparticles Decorated on Nitrogen-Doped Carbon Sheets for Boosted Lithium Storage Performance. *Chem. Eng. J.* 354, 172–181. doi:10.1016/j.cej.2018.08.024

Li, J., Yan, D., Lu, T., Yao, Y., and Pan, L. (2017). An Advanced CoSe Embedded within Porous Carbon Polyhedra Hybrid for High Performance Lithium-Ion and Sodium-Ion Batteries. *Chem. Eng. J.* 325, 14–24. doi:10.1016/j.cej.2017.05.046

Li, J., Zhuang, N., Xie, J., Li, X., Zhuo, W., Wang, H., et al. (2020). K-Ion Storage Enhancement in Sb 2 O 3/Reduced Graphene Oxide Using Ether-Based Electrolyte. *Adv. Energ. Mater.* 10 (5), 1903455. doi:10.1002/aenm.201903455

Li, K., Zhang, J., Lin, D., Wang, D.-W., Li, B., Lv, W., et al. (2019). Evolution of the Electrochemical Interface in Sodium Ion Batteries with Ether Electrolytes. *Nat. Commun.* 10 (1), 725. doi:10.1038/s41467-019-08506-5

Li, R., Xing, L., Chen, A., Zhang, X., Kong, A., and Shan, Y. (2019). Covalent Organic Polymer-Derived Carbon Nanotube-Twined Carbon Nanospheres for Efficient Oxygen Electroreduction and Capacitance Storage. *Ionics* 26 (2), 927–937. doi:10.1007/s11581-019-03277-x

Li, T., and Zhang, Q. (2018). Advanced Metal Sulfide Anode for Potassium Ion Batteries. *J. Energ. Chem.* 27 (2), 373–374. doi:10.1016/j.jechem.2017.12.009

Li, X., Liu, Z., Li, J., Lei, H., Zhuo, W., Qin, W., et al. (2021). Insights on the Mechanism of Na-Ion Storage in Expanded Graphite Anode. *J. Energ. Chem.* 53, 56–62. doi:10.1016/j.jechem.2020.05.022

Li, X., Yin, X., Liang, S., Li, M., Cheng, L., and Zhang, L. (2019). 2D Carbide MXene Ti2CTX as a Novel High-Performance Electromagnetic Interference Shielding Material. *Carbon* 146, 210–217. doi:10.1016/j.carbon.2019.02.003

Li, Y., Liu, Y., Wang, M., Xu, X., Lu, T., Sun, C. Q., et al. (2018). Phosphorus-doped 3D Carbon Nanofiber Aerogels Derived from Bacterial-Cellulose for Highly-Efficient Capacitive Deionization. *Carbon* 130, 377–383. doi:10.1016/j.carbon.2018.01.035

Liu, T., Zhang, Y., Chen, C., Lin, Z., Zhang, S., and Lu, J. (2019). Sustainability-inspired Cell Design for a Fully Recyclable Sodium Ion Battery. *Nat. Commun.* 10 (1), 1965. doi:10.1038/s41467-019-09933-0

Lu, T., Liu, Y., Xu, X., Pan, L., Alothman, A. A., Shapter, J., et al. (2021). Highly Efficient Water Desalination by Capacitive Deionization on Biomass-Derived Porous Carbon Nanoflakes. *Sep. Purif. Tech.* 256, 117771. doi:10.1016/j.seppur.2020.117771

Sun, H., Li, J., Wang, W., Wang, Z., and Pan, L. (2021). Facile Iin-Ssitu Synthesis of Heazlewoodite on Nitrogen-Doped Reduced Graphene Oxide for Enhanced Sodium Storage. *J. Colloid Interf. Sci.* 594, 35–46. doi:10.1016/j.jcis.2021.03.047

Wan, L., Tang, Y., Chen, L., Wang, K., Zhang, J., Gao, Y., et al. (2021). In-situ Construction of G-C3N4/Mo2CTx Hybrid for superior Lithium Storage with Significantly Improved Coulombic Efficiency and Cycling Stability. *Chem. Eng. J.* 410, 128349. doi:10.1016/j.cej.2020.128349

Wang, J.-G., Liu, H., Zhou, R., Liu, X., and Wei, B. (2019). Onion-like Nanospheres Organized by Carbon Encapsulated Few-Layer MoS2 Nanosheets with Enhanced Lithium Storage Performance. *J. Power Sourc.* 413, 327–333. doi:10.1016/j.jpowsour.2018.12.055

Wang, K., Liu, Y., Ding, Z., Chen, Z., Zhu, G., Xu, X., et al. (2021). Controlled Synthesis of NaTi2(PO4)3/Carbon Composite Derived from Metal-Organic-Frameworks as Highly-Efficient Electrodes for Hybrid Capacitive Deionization. *Sep. Purif. Tech.* 278, 119565. doi:10.1016/j.seppur.2021.119565

Wang, L., Wang, J., Guo, F., Ma, L., Ren, Y., Wu, T., et al. (2018). Understanding the Initial Irreversibility of Metal Sulfides for Sodium-Ion Batteries via Operando Techniques. *Nano Energy* 43, 184–191. doi:10.1016/j.nanoen.2017.11.029

Wang, N., Wang, Y., Xu, X., Liao, T., Du, Y., Bai, Z., et al. (2018). Defect Sites-Rich Porous Carbon with Pseudocapacitive Behaviors as an Ultrafast and Long-Term Cycling Anode for Sodium-Ion Batteries. *ACS Appl. Mater. Inter.* 10 (11), 9353–9361. doi:10.1021/acsami.7b17893

Wang, T., Legut, D., Fan, Y., Qin, J., Li, X., and Zhang, Q. (2020). Building Fast Diffusion Channel by Constructing Metal Sulfide/Metal Selenide Heterostructures for High-Performance Sodium Ion Batteries Anode. *Nano Lett.* 20 (8), 6199–6205. doi:10.1021/acs.nanolett.0c02595

Xie, J., Li, J., Li, X., Lei, H., Zhuo, W., Li, X., et al. (2020). Ultrahigh "Relative Energy Density" and Mass Loading of Carbon Cloth Anodes for K-Ion Batteries. *CCS Chem.* 3 (2), 791–799. doi:10.31635/ccschem.020.202000203

Xie, J., Li, X., Lai, H., Zhao, Z., Li, J., Zhang, W., et al. (2019). A Robust Solid Electrolyte Interphase Layer Augments the Ion Storage Capacity of Bimetallic-Sulfide-Containing Potassium-Ion Batteries. *Angew. Chem.* 131 (41), 14882–14889. doi:10.1002/ange.201908542

Yang, J., Li, J., Wang, T., Notten, P. H. L., Ma, H., Liu, Z., et al. (2021). Novel Hybrid of Amorphous Sb/N-Doped Layered Carbon for High-Performance Sodium-Ion Batteries. *Chem. Eng. J.* 407, 127169. doi:10.1016/j.cej.2020.127169

Zhang, X., Han, L., Li, J., Lu, T., Li, J., Zhu, G., et al. (2022). A Novel Sn-Based Coordination Polymer with High-Efficiency and Ultrafast Lithium Storage. *J. Mater. Sci. Tech.* 97, 156–164. doi:10.1016/j.jmst.2021.04.045

Zhang, X., Li, J., Li, J., Han, L., Lu, T., Zhang, X., et al. (2020). 3D TiO2@nitrogen-Doped carbon/Fe7S8 Composite Derived from Polypyrrole-Encapsulated Alkalized MXene as Anode Material for High-Performance Lithium-Ion Batteries. *Chem. Eng. J.* 385, 123394. doi:10.1016/j.cej.2019.123394

Zhang, X., Yao, L., Liu, S., Zhang, Q., Mai, Y., Hu, N., et al. (2018). High-performance Lithium Sulfur Batteries Based on Nitrogen-Doped Graphitic Carbon Derived from Covalent Organic Frameworks. *Mater. Today Energ.* 7, 141–148. doi:10.1016/j.mtener.2018.01.003

Zhang, X., Zhu, G., Wang, M., Li, J., Lu, T., and Pan, L. (2017). Covalent-organic-frameworks Derived N-Doped Porous Carbon Materials as Anode for superior Long-Life Cycling Lithium and Sodium Ion Batteries. *Carbon* 116, 686–694. doi:10.1016/j.carbon.2017.02.057

Zhang, Y., Li, J., Gong, Z., Xie, J., Lu, T., and Pan, L. (2021). Nitrogen and Sulfur Co-doped Vanadium Carbide MXene for Highly Reversible Lithium-Ion Storage. *J. Colloid Interf. Sci.* 587, 489–498. doi:10.1016/j.jcis.2020.12.044

Zhang, Y., Li, J., Li, H., Shi, H., Gong, Z., Lu, T., et al. (2022). Facile Self-Assembly of Carbon-free Vanadium Sulfide Nanosheet for Stable and High-Rate Lithium-Ion Storage. *J. Colloid Interf. Sci.* 607 (Pt 1), 145–152. doi:10.1016/j.jcis.2021.08.192

Zhang, Y., Li, J., Ma, L., Li, H., Xu, X., Liu, X., et al. (2022). Insights into the Storage Mechanism of 3D Nanoflower-like V3S4 Anode in Sodium-Ion Batteries. *Chem. Eng. J.* 427, 130936. doi:10.1016/j.cej.2021.130936

Zheng, S., Li, Q., Xue, H., Pang, H., and Xu, Q. (2020). A Highly Alkaline-Stable Metal Oxide@metal-Organic Framework Composite for High-Performance Electrochemical Energy Storage. *Nat. Sci. Rev.* 7 (2), 305–314. doi:10.1093/nsr/nwz137

Zou, K., Cai, P., Wang, B., Liu, C., Li, J., Qiu, T., et al. (2020). Insights into Enhanced Capacitive Behavior of Carbon Cathode for Lithium Ion Capacitors: The Coupling of Pore Size and Graphitization Engineering. *Nano-micro Lett.* 12 (1), 121. doi:10.1007/s40820-020-00458-6

Conflict of Interest: HS, QH, and HW were employed by Beijing Smart-Chip Microelectronics Technology Co., Ltd. XiZ, ZZ and XuZ were employed by State Grid Beijing Chaoyang Electric Power Supply Company.